

# Correlation Study of CFD Turbulence Modeling Approaches for an Axisymmetric Missile Concept

Ross B. Alexander<sup>1</sup>, Gregory Z. McGowan<sup>2</sup>  
*Corvid Technologies LLC, Mooresville, NC 28117-8006*

A correlation study for aerodynamic coefficient estimation of an axisymmetric missile concept with cruciform strakes and inline tail fins for a range of Mach numbers and angles of attack using a variety of computational fluid dynamic (CFD) turbulence modeling approaches has been completed. The principal geometry examined in this study was the Configuration 2 missile concept, detailed in a NASA Langley Research Center (NASA-LRC) report. Standard six-degree-of-freedom aerodynamic coefficients were predicted for four different CFD turbulence modeling approaches using the proprietary state-of-the-art RavenCFD Navier-Stokes flow solver. The data obtained from computational fluid dynamic methods are compared against NASA-LRC experimental wind tunnel results. In general, the CFD turbulence modeling approaches demonstrate good agreement with experimental data. Notable discrepancies exist between CFD methodologies and experimental data for pitching moment coefficients, likely due to experimental error. An optimal turbulence modeling approach for missilelike geometries in subsonic, transonic, and low supersonic flow at small-to-moderate angles of attack is a detached-eddy simulation (DES) with the shear stress transport turbulence model with rotation and curvature correction (SST-RC).

## Nomenclature

$A_{ref}$	=	maximum body cross-section area, in <sup>2</sup>
$C_A$	=	configuration axial-force coefficient with base axial-force coefficient removed
$C_{A, base}$	=	base axial-force coefficient
$C_{A, raw}$	=	configuration axial-force coefficient
$C_l$	=	configuration rolling-moment coefficient
$C_m$	=	configuration pitching-moment coefficient shifted 1.75 in. upstream
$C_{m, raw}$	=	configuration pitching-moment coefficient
$C_n$	=	configuration yawing-moment coefficient
$C_N$	=	configuration normal-force coefficient
$C_Y$	=	configuration side-force coefficient
$D$	=	maximum body diameter, in
$F_A$	=	configuration axial force, lbf
$F_N$	=	configuration normal force, lbf
$F_Y$	=	configuration side force, lbf
$L$	=	body length, in
$M_\infty$	=	free-stream Mach number
$M_l$	=	configuration rolling moment, in-lbf
$M_m$	=	configuration pitching moment, in-lbf
$M_n$	=	configuration yawing moment, in-lbf
$p_\infty$	=	free-stream static pressure, psi
$q_\infty$	=	free-stream dynamic pressure, psi
$T_\infty$	=	free-stream static temperature, R
$\alpha$	=	configuration angle of attack, deg
$\alpha_i$	=	initial configuration angle of attack, deg
$\alpha_f$	=	final configuration angle of attack, deg
$\beta$	=	configuration sideslip angle, deg
$\delta$	=	roll control deflection, deg
$\zeta$	=	vorticity, s <sup>-1</sup>
$\iota$	=	b-plane steering control deflection, deg
$\iota'$	=	a-plane steering control deflection, deg
$\phi$	=	configuration roll angle, deg

<sup>1</sup> Aerospace Engineering Intern, 145 Overhill Drive. Student, Texas A&M University.

<sup>2</sup> Aerospace Engineer, 145 Overhill Drive. Member AIAA.

## I. Introduction

### A. Aerodynamic Coefficient Prediction Methods

Evaluation of the principal six-degree-of-freedom aerodynamic coefficients is critical in missile trajectory estimation, control system design, and the overall performance of the design. Discrepancies between predicted and actual aerodynamic coefficients can lead to control algorithms and trajectory estimation algorithms that produce spurious results. To reduce the risk of errors, several methods are frequently employed in obtaining these coefficients. Typically, there are three methods for acquiring these data – i.) empirical flight testing; ii.) experimental wind tunnel testing; and iii.) computational fluid dynamic (CFD) simulation.

While empirical flight test data can be the most useful and accurate way to obtain data about a given flight configuration, it is often the least feasible. Despite obtaining accurate empirical data, flight testing is very resource-intensive. Flight testing often requires a full-scale operational model, as well as extended periods of testing time, large testing areas, and numerous personnel. For designs that have not been validated, flight testing may also be unsafe. Instrumentation and sensing difficulties can also hinder data acquisition in full-scale flight testing.

Experimental wind tunnel testing is another useful tool to obtain data, but the data produced can be full of inaccuracies. Wind tunnel testing is one of the more accessible tools for acquiring aerodynamic coefficient data and does not require a full-scale operational design, which is a significant benefit over an empirical flight test. However, wind tunnel testing can also be time-consuming and expensive depending of the size of the aerodynamic test matrix and the capabilities of the wind tunnel facilities.

Rapidly advancing modern computational power and parallelization has given way to CFD simulation becoming a modern and economical tool for iterative design and testing. The rapid development of CFD in the last several decades has led to significant advances in accuracy, but data from a CFD simulation can be full of errors if simulation parameters are not judiciously prescribed. CFD simulations require no physical model – which is a benefit over both empirical flight testing and wind tunnel testing – and solutions may be obtained in a matter of weeks to months. However, computational power can be expensive. Another difficulty of CFD is the selection of appropriate models and approximations to govern the simulation – there are numerous solution techniques to select and not all may be best for a given problem. For turbulent flows, there are several solution approaches, which include: Reynolds-averaged Navier-Stokes (RANS) equations solution, detached-eddy simulation (DES), large-eddy simulation (LES), and direct numerical simulation (DNS).

### B. CFD Solution Approaches

The RANS equations solution approach approximates the mean flow characteristics through Reynolds-averaging. However, in developing the RANS approximation, several quantities, known as Reynolds stresses, are introduced. Additional sets of equations, known as turbulence models,

provide the necessary and sufficient closure of the RANS equations.

Over the last few decades, several turbulence models have come into modern usage. Modifications and corrections have been developed for some of these models and can lead to improvements under given flow conditions, such as vortex shedding or strong streamline curvature. Each turbulence model has advantages and disadvantages and care should be taken when selecting an appropriate turbulence model for the design problem. Solving the RANS equations is computationally cheap when compared to other methods and often provides the level of information necessary for most engineering design problems.

The DES solution approach is a hybrid RANS/LES approach, combining large-eddy modeling in fine grid regions, while utilizing the RANS model in coarser grid regions [1]. If the largest cell dimension is *smaller* than the local turbulent length scale, the cell is modeled using LES techniques with a subgrid-scale formulation first proposed by Smagorinsky [2] – *large eddies are modeled in these regions*. If the largest cell dimension is *larger* than the local turbulent length scale, the cell is modeled using RANS techniques – *large eddies are not modeled in these regions*.

DES provides a trade-off between computational expense and turbulent eddy resolution with RANS and LES modeling approaches. Compared to the RANS turbulence modeling approach, DES is more accurate, but computationally more expensive; compared to LES, DES is less accurate, but computationally cheaper.

LES models the entire domain down to a specified filter cutoff size, after which, turbulent eddies are approximated using the Smagorinsky model [2]. Overall, LES requires a finer grid and smaller timestep than a RANS or DES solution approach, which increases the computational cost, but provides a finer resolution of turbulent eddies in the simulation domain.

DNS resolves the entire Navier-Stokes equations without applying a turbulence model or a time-averaged solution. DNS requires the use of a grid that is everywhere smaller the turbulent dissipation length scale, or Kolmogorov scale [3]. Additionally, DNS requires a timestep that is less than the smallest timescale of turbulent activity. In this regard, DNS solutions are incredibly accurate, but require so much computational power that DNS is cost-prohibitive for typical engineering applications. A typical DNS solution may take months or years to compute and provides more information than necessary for most engineering applications, such as aerodynamic coefficient prediction, so its primary use is in turbulence research.

### C. Correlation Study

In predicting the six-degree-of-freedom aerodynamic coefficients, it is important to acquire multiple datasets using a variety of testing methods and perform a correlation study to determine the accuracy of the selected methods against each other. It is the focus of this study to examine the correlation between an existing experimental wind tunnel dataset, provided in a NASA-LRC report [4], and four new computational datasets generated with a state-of-the-art CFD flow solver. Each computational dataset was generated using a different turbulence modeling approach – three datasets were generated using a Reynolds-averaged Navier-Stokes (RANS) solution approach

and one dataset was generated using a detached-eddy simulation (DES) solution approach.

## II. Geometric Model

The geometry considered in this study was the Configuration 2 (SN-SS-T) missile concept detailed in the NASA-LRC report [4]. Configuration 2 (SN-SS-T) consists of modular components designated in the report as: small nose (SN), short strakes (SS), and tails on (T). Model dimensions were provided and used to generate a 3D-CAD geometric model of the missile concept, depicted in Figs. 1 and 2. The missile concept has a tangent ogive nose that leads into a long cylindrical section connected to the main body by a boattail. On the main body, there are four strake mounting pads arranged in an axisymmetric configuration, used in the reported wind tunnel test to provide a smooth contact surface between the body and the strake. Four strakes are mounted on external surface of the mounting pads. Aft of the strake mounting pads are four tail fins arranged in an axisymmetric configuration in-line with the four strakes. A boattail is attached to the end of the main body section.

For the missile concept, the main body diameter is 3.150 in and the model length is 42.528 in. The maximum frontal area is 7.793 in<sup>2</sup>. These three values represent the characteristic coefficient reduction parameters  $D$ ,  $L$ , and  $A_{ref}$ , respectively. A table of relevant geometric parameters is included in Table 1.

Mesh generation was accomplished using the Pointwise grid generation software. An unstructured, triangular surface mesh was developed with grid refinements at leading and trailing edges of the fins and strakes and in other flowfield locations with strong predicted gradients. Additionally, 2D quadrilateral cells were generated on the leading edges of the strakes. An unstructured tetrahedral volume mesh was developed using a spherical farfield with approximately 20 body-lengths radius (800 in). To resolve the viscous sublayer on the body, prismatic

**Table 1. Geometric Model Parameters**

Parameter	Value
Nose diameter	2.694 in
Nose boattail angle	3.367 deg
Maximum frontal area	7.793 in <sup>2</sup>
Body diameter	3.150 in
Strake root chord	9.592 in
Strake tip chord	5.040 in
Strake span	1.173 in
Tail fin root chord	1.992 in
Tail fin tip chord	1.213 in
Tail fin span	1.953 in
Base boattail angle	2.297 deg
Base diameter	3.040 in

cells were generated on wall surfaces and allowed to grow into pyramidal cells as necessary. A single frustum-shaped source was placed around the body of the missile concept and the wake to increase near-body and wake refinement. Measures of grid consistency and quality, such as volume ratio, equiangle skewness, and aspect ratio, were optimized using built-in Pointwise algorithms. The refined mesh contained approximately 35 million cells – consisting of approximately 30 million tetrahedral cells, 5 million prismatic cells, and 100 thousand pyramidal cells. The surface mesh and volume mesh are shown in Figs. 3 and 4, respectively.

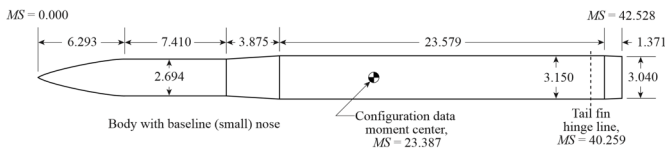


**Figure 1. Configuration 2 – Drawing**

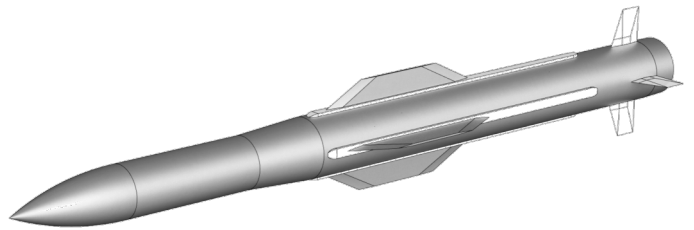


**Figure 2. Configuration 2 - 3D CAD**

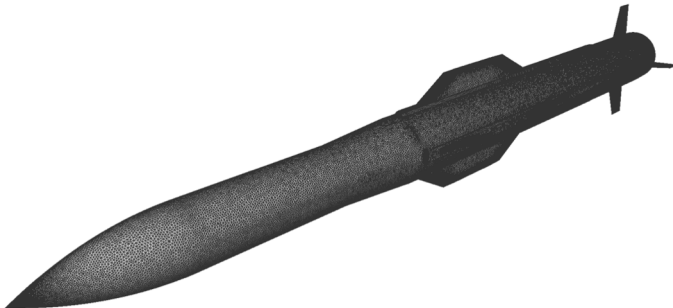


**Figure 3. Configuration 2 - Surface Mesh**

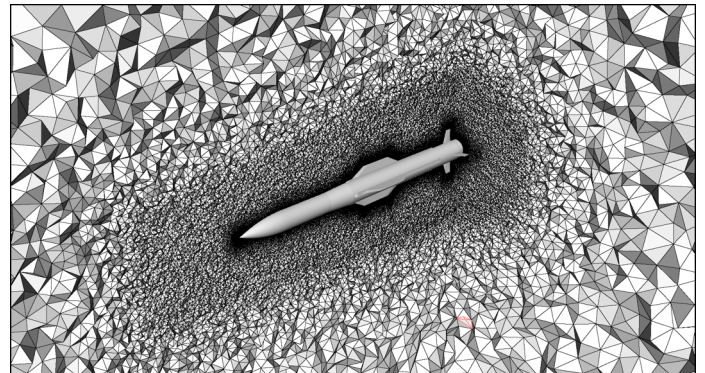


**Figure 4. Configuration 2 - Volume Mesh**

### III. Computational Approach

#### A. RavenCFD

The state-of-the-art RavenCFD Reynolds-averaged Navier-Stokes solver developed at Corvid Technologies was used for all CFD flow solutions discussed herein. RavenCFD is an arbitrary polyhedral, unstructured flow solver that uses an unconditionally stable point implicit scheme. RavenCFD uses a cell-centered finite volume approach with a variety of flux schemes, gradient calculation methods, and turbulence models. Temporal accuracy of the RavenCFD solver can be set to first-order or second-order as requested. RavenCFD supports a wide variety of boundary conditions. The solver has shown linear to superlinear efficiency on thousands of processors. RavenCFD maintains a variety of additional capabilities including: grid adaptation, grid deformation and optimization, immersed-boundary methods, rigid body motion, six-degree-of-freedom equations of motion. In this study, the traditional static run capability and the rigid body motion (RBM) capability were utilized extensively.

The traditional RavenCFD static run capability allows for flow solution at specified static conditions. The RavenCFD RBM capability allows for prescribed rigid body motion parameters capable of simulating a wind-tunnel roll, pitch, or yaw sweep. Typically, for an angular sweep, the computational grid is rotated at a constant angular acceleration until a prescribed angular displacement and angular velocity is reached. Then, the grid is rotated at a constant angular velocity until the completion of the RBM run.

#### B. Static and Rigid Body Runs

In the case of this study, a static run was initialized at  $\alpha = -7$  deg for a specified Mach number. The static run was prescribed a global timestep of 100  $\mu$ s and *one* Newton subiteration. Second-order spatial accuracy and first-order temporal accuracy were used with a least-squares gradient formulation and the low-diffusion flux-splitting scheme [5]. The static run was iterated to convergence and the flow solver was terminated.

The static flow solution developed earlier was used as the initial condition for the RBM run for the same specified Mach number. The RBM run was prescribed a global timestep of 1 ms and *two* Newton subiterations. Second-order spatial accuracy and second-order temporal accuracy were used with a least-squares gradient formulation and the low-diffusion flux-splitting scheme [5], as before. The RavenCFD flow solver was invoked with rigid body motion parameters and the grid was accelerated in a pitch sweep from rest at  $\alpha = -7$  deg to an angular velocity of 5 deg/s at  $\alpha = -6$  deg. At  $\alpha = -6$  deg, the rigid body motion parameters applied a constant angular velocity of 5 deg/s until  $\alpha = 23$  deg, at which point the flow solver was terminated. Using a global timestep of 1 ms, the angular-iterative resolution is

0.005 deg/iteration or 200 iteration/deg. The rigid body motion parameters are tabulated in Table 2.

Table 2. Rigid Body Motion Parameters

Initial Angle	Final Angle	Angular Displacement	Angular Velocity	Angular Acceleration
-7 deg	-6 deg	+1 deg	<i>linear ramp</i>	12.5 deg/s <sup>2</sup>
-6 deg	23 deg	+29 deg	5 deg/s	0 deg/s <sup>2</sup>

#### C. Turbulence Modeling Approaches

The principal focus of this study was the evaluation of a variety of solution techniques and turbulence models. Three Reynolds-averaged Navier-Stokes (RANS) turbulence modeling approaches were used – each with different turbulence models. Additionally, a single detached-eddy simulation (DES) turbulence modeling approach was used with one turbulence model. Turbulence modeling approaches were kept constant between corresponding static and rigid body motion runs. The selected modeling approaches are tabulated in Table 3 and a complete run matrix is included in Appendix A.

The first modeling approach selected was a RANS equations solution coupled with the Spalart-Allmaras turbulence model with the Dacles-Mariani modification [6, 7] (DMSA). The DMSA model is typically used in aerodynamics applications and provides good flow resolution while maintaining numerical stability. The second modeling approach was a RANS equations solution coupled with the Menter  $k-\omega$  Baseline turbulence model [8] with the rotation and curvature correction (BSL-RC). The BSL-RC model performs well in prediction of the flow separation in the near-field. The third modeling approach was a RANS equations solution coupled with the Menter  $k-\omega$  Shear Stress Transport turbulence model with the rotation and curvature correction (SST-RC) [9]. The SST-RC model provides an advantage over the BSL-RC turbulence model by including transport effects of eddy-viscosity and providing high levels of accuracy for boundary layer prediction. The final turbulence modeling approach was a DES solution coupled with the Menter  $k-\omega$  Shear Stress Transport turbulence model with the rotation and curvature correction (DES-SST-RC). This modeling approach was selected as DES can often improve the accuracy of the results for the axial force coefficient for the massively-separated flow at the base of the missile. The DES-SST-RC turbulence modeling approach selected uses the zonal  $F_2$  blending function from the SST model [9].

Table 3. Selected Turbulence Modeling Approaches

Nomenclature	Solution Technique	Turbulence Model
DMSA	RANS	Spalart-Allmaras with Dacles-Mariani Modification
BSL-RC	RANS	$k-\omega$ Baseline with Rotation/Curvature Correction
SST-RC	RANS	$k-\omega$ Shear Stress Transport with Rotation/Curvature Correction
DES-SST-RC	DES	$k-\omega$ Shear Stress Transport with Rotation/Curvature Correction

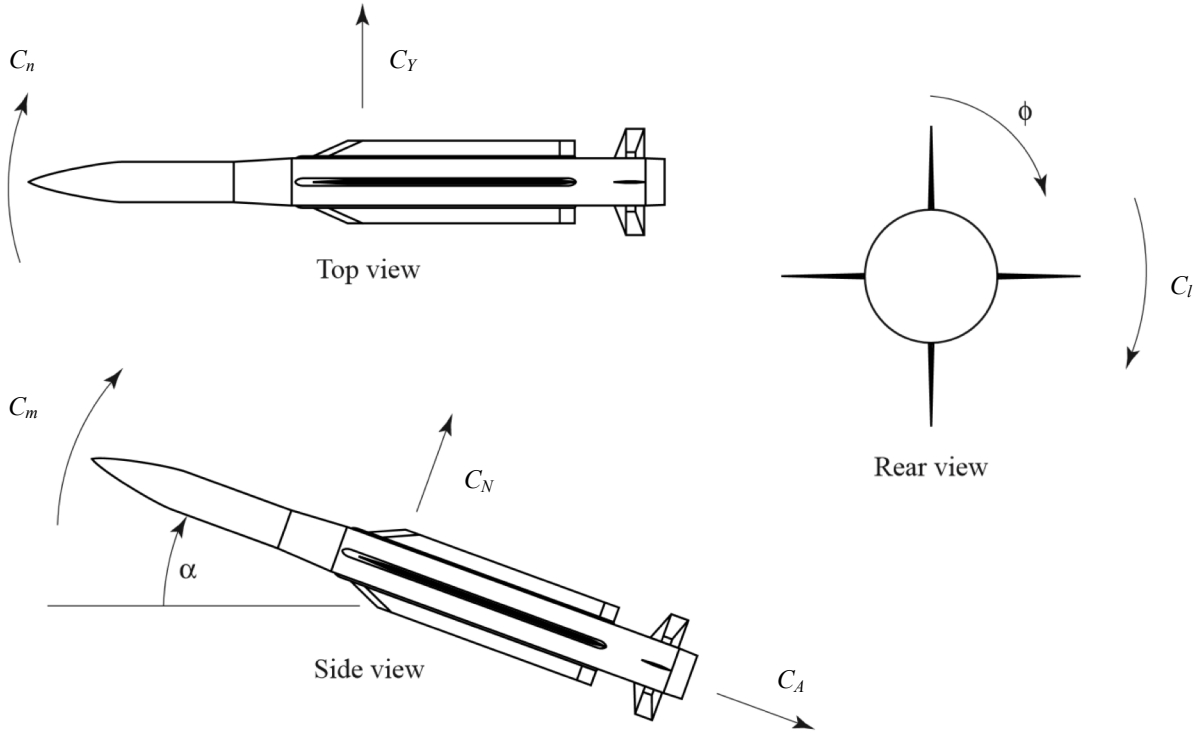


Figure 5. Force and Moment Reporting Convention (Allen, 2005)

#### D. Aerodynamic Coefficient Calculation and Reporting

Aerodynamic coefficients from the both the NASA-LRC wind tunnel test and RavenCFD simulations are reported using the PANAIR convention, as depicted in Fig. 5. The origin is located on the center of the base (rear) with the  $x$ -,  $y$ -, and  $z$ -axis aligned with  $C_A$ ,  $C_Y$ , and  $C_N$ , respectively (Fig. 5).

Standard six-degree-of-freedom aerodynamic coefficients are computed by non-dimensionalizing the forces and moments by geometric and flow parameters as follows:

$$C_A = \frac{F_A}{q_\infty A_{ref}} \quad (1)$$

$$C_Y = \frac{F_Y}{q_\infty A_{ref}} \quad (2)$$

$$C_N = \frac{F_N}{q_\infty A_{ref}} \quad (3)$$

$$C_l = \frac{-M_l}{q_\infty A_{ref} D} \quad (4)$$

$$C_m = \frac{M_m}{q_\infty A_{ref} D} \quad (5)$$

$$C_n = \frac{-M_n}{q_\infty A_{ref} D} \quad (6)$$

Note that Eqns. 1-6 are defined to match the convention depicted in Fig. 5 – a positive rolling moment indicates roll-

right, positive pitching moment indicates nose-up, and positive yawing moment indicates nose-right.

In the NASA-LRC wind tunnel test data, the  $C_A$  contribution from the wind tunnel sting was removed. This was duplicated in the CFD results presented here by subtracting the axial force coefficient contribution of the base patch ( $C_{A,base}$ ) from the total configuration axial force coefficient ( $C_{A,total}$ ). The values reported herein are labeled  $C_A$ , with the base contribution removed, as shown in the equation below:

$$C_A = C_{A,total} - C_{A,base} \quad (7)$$

$C_m$  values reported in the NASA-LRC wind tunnel test showed significant discrepancy from preliminary RavenCFD predictions and Missile DATCOM for identical conditions. Since Missile DATCOM and RavenCFD results agree well with one another, it was assumed that the wind tunnel test data were incorrectly reported or that there was an internal sting misalignment. Accordingly, the assumption was made that the actual configuration data moment center was approximately 1.75 in upstream of the specified configuration data moment center. The transfer distance of 1.75 in, however, was purely arbitrary and no physical or meaningful correlation could be made to isolate the source of experimental error. The Missile DATCOM and RavenCFD comparison and  $C_m$  correction is described in further detail in the Results section.

The NASA-LRC data are reproduced exactly as reported and are labeled  $C_m$ . The RavenCFD values reported herein are also labeled  $C_m$ , but have been shifted 1.75 in upstream from the NASA-LRC-reported configuration data moment center of

23.387 in aft of the nose to 21.637 in aft of the nose. The moment center transfer was applied on the raw RavenCFD pitching moment coefficient ( $C_{m,raw}$ ) to yield the adjusted pitching moment coefficient ( $C_m$ ) using the following equation:

$$C_m = C_{m,raw} - \frac{1.75}{D} C_N \quad (8)$$

It should be noted that the NASA-LRC wind tunnel tests took place in two different wind tunnels. For  $0.60 < M_\infty < 1.18$ , tests took place in the NASA-LRC 8-ft Transonic Pressure Tunnel (TPT), while for  $1.70 < M_\infty < 4.63$ , tests took place in the NASA-LRC Unitary Plan Wind Tunnel (UPWT) [5].

For the results presented here, sixteen different RavenCFD simulations were completed – each individual simulation consisted of a static run and rigid body run paired together with identical conditions. Angle of attack sweeps were completed for a specified Mach number. The primary run matrix consisted of two variables,  $M_\infty$  and the turbulence modeling approach. In the results presented here, Mach numbers 0.60, 0.90, 1.18, and 2.00 and the DMSA, BSL-RC, SST-RC, and DES-SST-RC turbulence modeling approaches were tested. Sideslip angle and roll angle were set to  $\beta = 0$  and  $\phi = 0$  for all runs. Fin deflection controls were set to  $\nu/\delta = 0/0/0$  for all runs, indicating no fin deflection. A test matrix describing the completed runs is included in Appendix A.

#### IV. Results

For each rigid body motion run, 6,200 data points were obtained across the range of -7 deg to 23 deg. For -7 deg to -6 deg, 400 unequally-spaced data points were obtained and for -6 deg to 23 deg, 5,800 equally-spaced data points were obtained. This unequal spacing for -7 deg to -6 deg can be attributed to the rigid body motion angular acceleration. The plotted data is sampled at every 10 data points. All plots comparing the six-degree-of-freedom aerodynamic coefficients and turbulence modeling approaches are included in Appendices B-G. All runs exhibited expected trends for the data.

##### A. Axial Force Coefficient Results

The axial force coefficients reported by NASA-LRC are reproduced here exactly, while the axial force coefficients reported by RavenCFD are the configuration axial force coefficients with the axial force coefficient contributions by the base removed. This is in accordance with the technique reported in the NASA-LRC study and described earlier and in Eqn. 7.

Results from subsonic and transonic runs indicate poor agreement with experimental data within the -5 deg to 5 deg angle of attack range. Above 5 deg angle of attack, the results of the subsonic and transonic runs show good agreement with experimental data for angles of attack. Results from the supersonic run give good agreement with the experimental data for the -5 deg to 5 deg angle of attack range, while poorer agreement is observed above 5 deg angle of attack.

In general, the DES-SST-RC case performs the best and removes some of the initial discrepancies in the low angle of attack range. At higher angles of attack, there is no clear optimal model as all perform well. However, the BSL-RC model tends

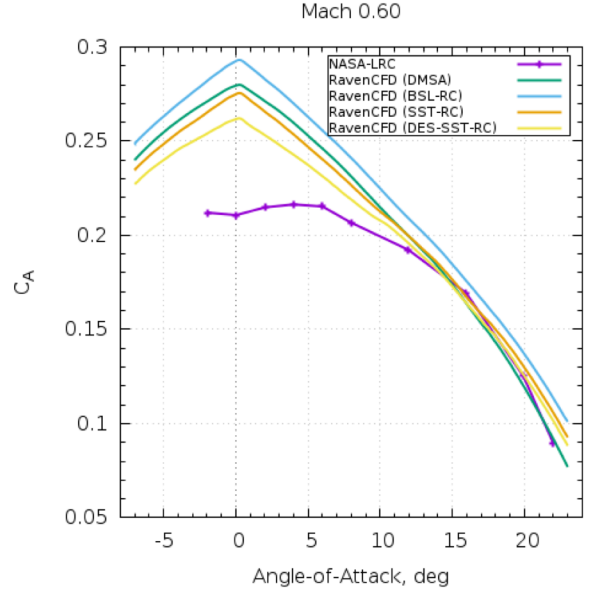


Figure 6. Axial Force Coefficient Results for Mach 0.60

to be the poorest predictor of  $C_A$  across the majority of the velocities and angles of attack tested.

It should be noted that theory suggests that the maximum value of  $C_A$  should be at 0 deg angle of attack. This result is seen in the data produced by RavenCFD, while NASA-LRC data typically indicates a peak  $C_A$  around or above 5 deg angle of attack.

The onset maximum  $C_A$  discrepancy and the initial  $C_A$  discrepancy from theoretical and computational perspectives appears to arise out of experimental error. The source of this error is unknown, but may likely stem from sting misalignments, nonlinear sting effects, or baseflow effects due to imbalanced cavity pressures. Additionally, the discrepancies between the axial force coefficient datasets may be exacerbated by potentially non-identical coefficient adjustments performed on the experimental and computational datasets.

At high angles of attack, all model exhibited excellent agreement with the NASA-LRC results.

##### B. Side Force Coefficient Results

In essentially all cases tested, each turbulence modeling approach performs nearly identically. Apart from some discrepancies between the data at Mach 0.90 and at high angles of attack, turbulence modeling approach effects are essentially indistinguishable. In the range of -5 deg to 10 deg angle of attack, RavenCFD predicts a near-zero side-force coefficient. All turbulence modeling approaches then predict some divergence from a near-zero side-force coefficient with the value of the coefficient largely dependent on the Mach number. Discrepancies between experimental data are observed for all cases, but errors in the experimental data are likely the principal cause for the discrepancies.

The side force coefficient should theoretically be zero for an axisymmetric missile with four strakes and fins, aligned with the coordinate axes. While missile *designs* may be unbiased, the actual *physical models* may contain small manufacturing defects



and uncontrollable geometric aberrations. In addition, wind tunnel sting alignment error may cause dispersions from nominal values. The sting misalignment and geometric error effects may be amplified in an angle of attack sweep as the model is susceptible to higher pressures and strengthened strake vortex effects due to the increased angle of attack and flow speed on the body.

One notable difference between the experimental dataset and the computational dataset is the inversion of trends. While the experimental dataset tends to indicate a positive trend, the computational dataset tends to indicate a negative trend. Possible sources of this error may again be geometric model bias.  $C_Y$  values are likely to be very sensitive to inherent geometric bias, and due to the necessary discretization of the computational domain, this bias is essentially unavoidable for unstructured computational grids, *even if a model maintains symmetries*. Construction of a higher-resolution grid is likely to eliminate this bias and improve solution fidelity, but at the expense of computation time.

In general, all the NASA-LRC experimental data shows a bias toward a positive side force coefficient with increasing angle of attack. For the discrete mesh developed for the RavenCFD simulations, the model indicates a bias toward a negative side force coefficient.

### C. Normal Force Coefficient Results

Each of the turbulence modeling approaches demonstrated outstanding agreement with experimental results across all tested Mach numbers and angles of attack. The DES-SST-RC turbulence modeling approach predicted marginally closer to the experimental data than all others. All turbulence modeling approaches became very slightly overpredictive at higher angles of attack ( $\alpha > 20$  deg).

### D. Rolling Moment Coefficient Results

The results of the rolling moment coefficients follow patterns similar to the side force coefficients. In nearly all cases, each of the turbulence modeling approaches perform nearly identical to each other. Differences between the turbulence modeling approaches are elucidated in the Mach 0.6 and Mach 0.9 cases. In these cases, the DES turbulence modeling approach deviates from the RANS turbulence modeling approaches, and in while not necessarily in agreement with the experimental data, give rise to deviations from zero rolling moment coefficient at high angles of attack, which could be due to strake and tail fin vortex effects. At higher Mach numbers, the performance of all turbulence modeling approaches is roughly equivalent. For all the cases, the rolling moment coefficient is near-zero and shows deviation at high angles of attack.

The rolling moment coefficient should theoretically be zero. But, like the side force coefficients, small errors and inaccuracies can cascade and produce results that are dispersed from nominal. The experimental data shows a bias toward a positive rolling moment coefficient, but the RavenCFD simulation data does not show a clear directional bias. In general, the RavenCFD rolling moment coefficients are quite small and of comparable order of magnitude to the experimental data. In this sense, the RavenCFD data are in good agreement with the NASA-LRC results.

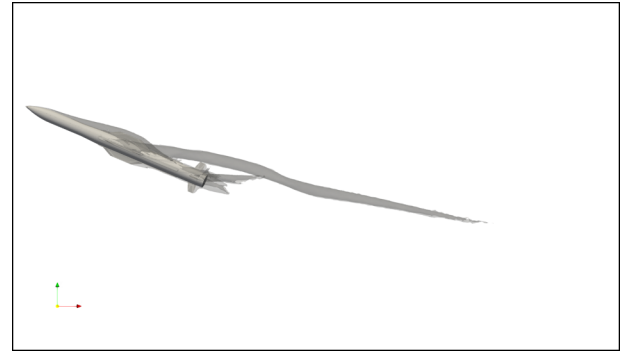


**Figure 7. Configuration 2 - Mach 0.90 Run with DMSA Turbulence Model - Vorticity Isosurface ( $|\zeta| = 3,000 \text{ s}^{-1}$ )**

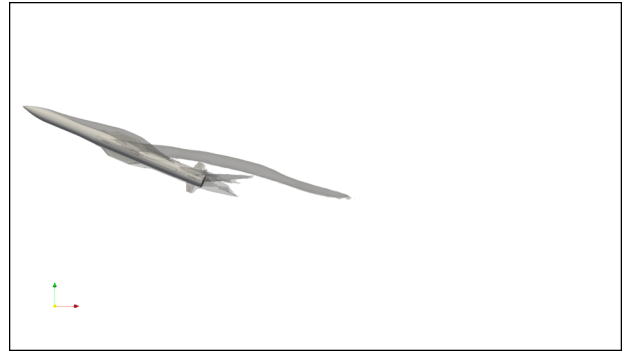


**Figure 8. Configuration 2 - Mach 0.90 Run with BSL-RC Turbulence Model - Vorticity Isosurface ( $|\zeta| = 3,000 \text{ s}^{-1}$ )**

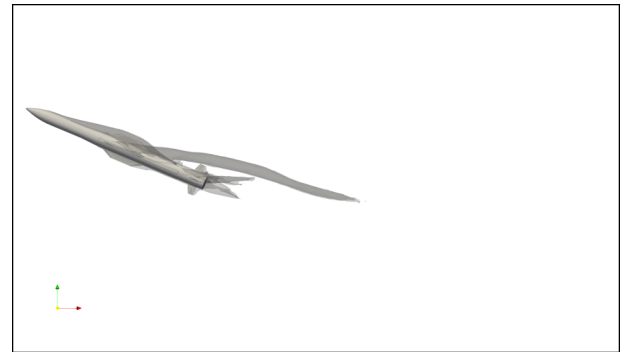


**Figure 9. Configuration 2 - Mach 0.90 Run with SST-RC Turbulence Model - Vorticity Isosurface ( $|\zeta| = 3,000 \text{ s}^{-1}$ )**

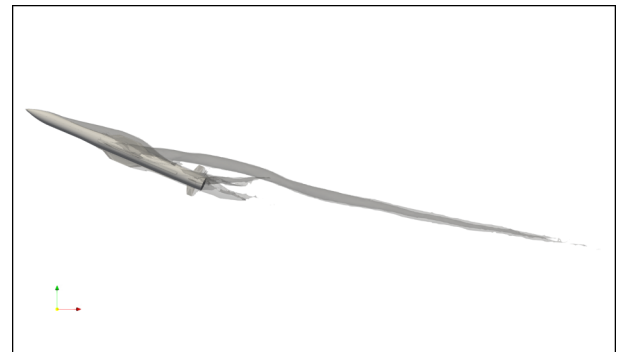


**Figure 10. Configuration 2 - Mach 0.90 Run with DES-SST-RC Turbulence Model - Vorticity Isosurface ( $|\zeta| = 3,000 \text{ s}^{-1}$ )**

### E. Pitching Moment Coefficient Results

The results of the pitching moment coefficient exhibited strong experimental agreement across low-to-moderate angles of attack ( $0 \text{ deg} < \alpha < 15 \text{ deg}$ ) for all Mach numbers tested. Turbulence models begin to diverge from the experimental results around  $15 \text{ deg}$  angle of attack. This has been shown to reduce pitching authority of the upper strake. Additionally, the Mach 2.0 case demonstrates poorer agreement around the  $0 \text{ deg}$  angle of attack range. This may be attributed to the pitching moment center correction.

In general, the SST-RC and DES-SST-RC turbulence models predict earlier divergence from experimental results, followed by the BSL-RC turbulence model, and the DMSA turbulence model, which for the conditions tested, generally follows the experimental data best.

### F. Yawing Moment Coefficient Results

The yawing moment coefficients predicted the theoretical near-zero values, while experimental data exhibited bias toward negative yawing moment coefficients. The computational model bias is not as severe as the experimental model bias, which can vary on average about two- to three-tenths of the yawing moment coefficient. The experimental data bias may also manifest itself into a gradient, with dependence on angle of attack. Thus, the experimental data is expected to include the effects of phantom yaw at high angles of attack.

### G. Other Results

While the aerodynamic coefficients were of principal importance in the study, a number of other effects were observed. It was found that strake-vortex formation had significant variance depending on the turbulence modeling approach. Figures 7-10 depict the missile concept at identical run conditions with vorticity isosurfaces ( $|\zeta| = 3,000 \text{ s}^{-1}$ ). It is observed that the DMSA and DES-SST-RC turbulence modeling approaches produced significantly longer vortices with considerably more strength, while the BSL-RC and SST-RC turbulence modeling approaches predicted significantly shorter, weaker vortical structures.

## V. Conclusion

Further work could be done to extend the application of this study to fin deflections and higher Mach numbers, and extreme angles of attack. Selection of a proper CFD turbulence modeling approach for missilelike geometries is critical in the accuracy of CFD simulations.

LES simulations, while would lend to improved solution accuracy, require immense computational resources that often preclude the use of an LES simulation. For missilelike geometries with a focus on aerodynamic coefficients at the tested Mach numbers and angles of attack, the optimal turbulence modeling approach is the detached-eddy simulation with shear stress transport turbulence model with rotation and curvature correction (DES-SST-RC). It is not known at this time if the same conclusion and modeling dependence holds for aerodynamic coefficients as functions of variables other than Mach number and angle of attack, given that fin deflections and roll angles were not explored. Additionally, the validity of turbulence models for missilelike geometries at extreme angles

of attack should be investigated. Run matrices with more expansive variable ranges would likely elucidate relationships of great interest.



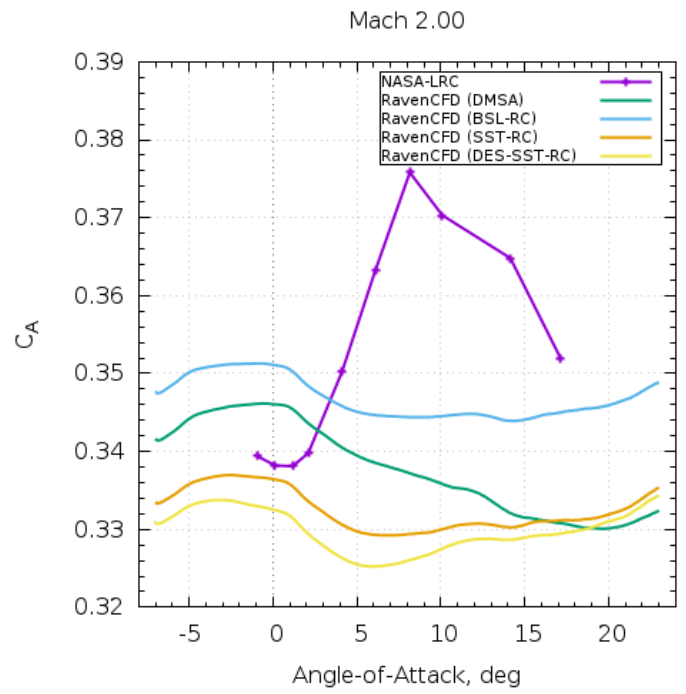
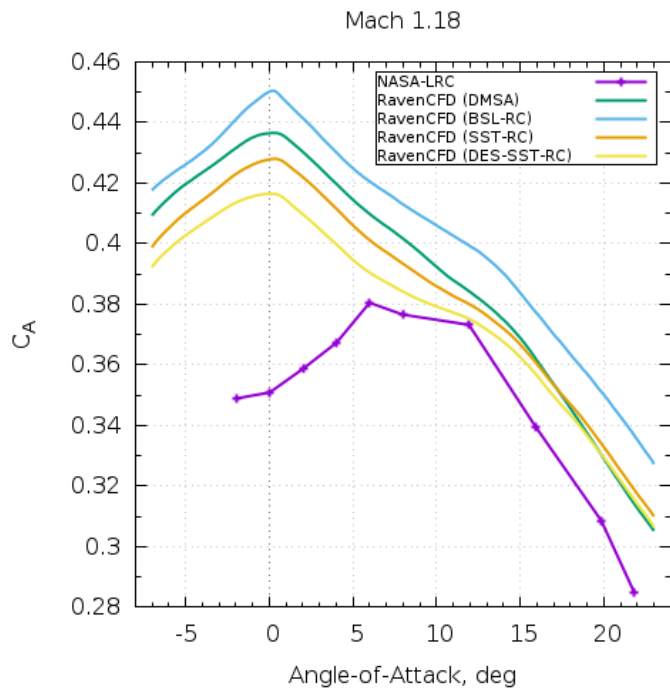
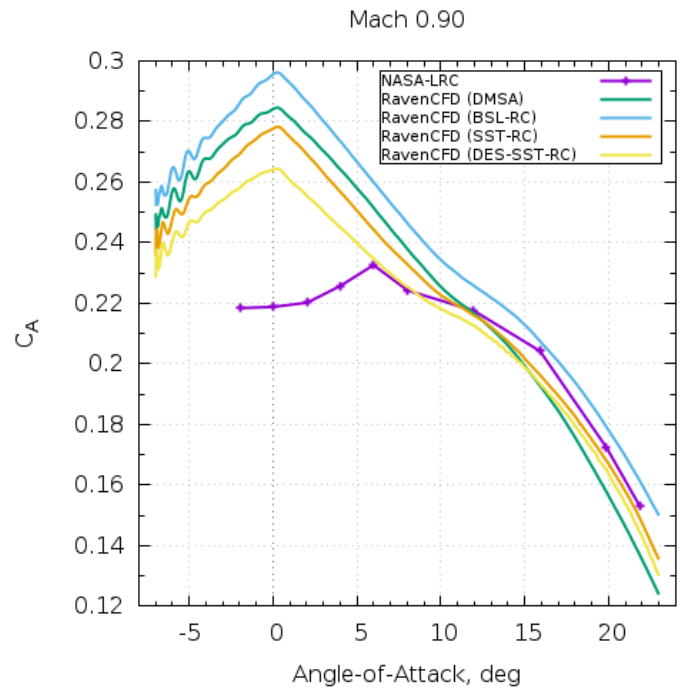
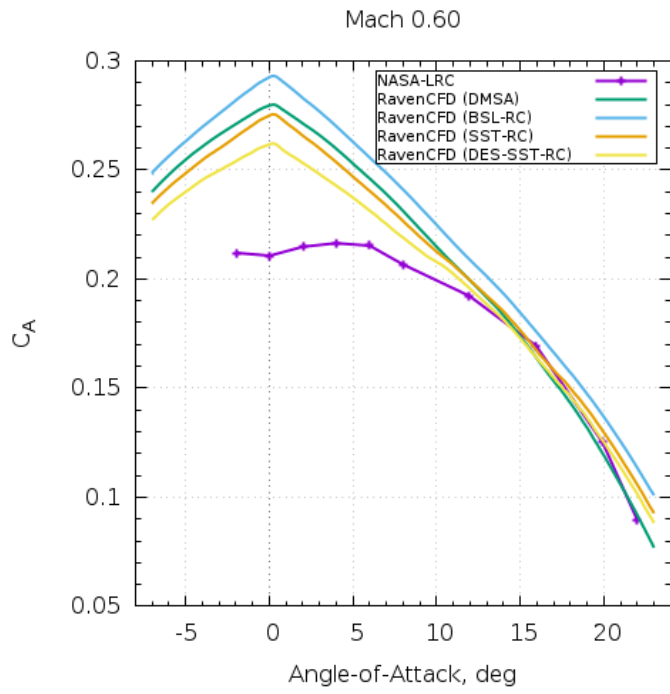
## Appendix

### A. Run Matrix

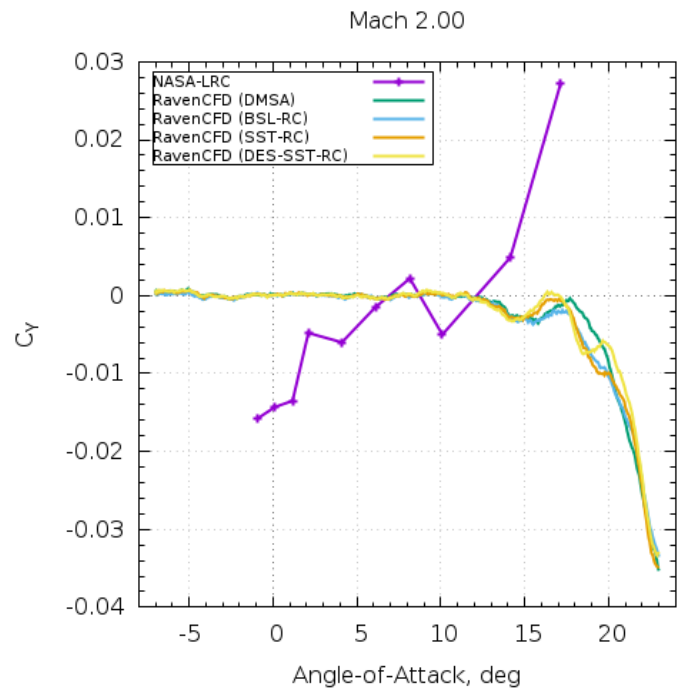
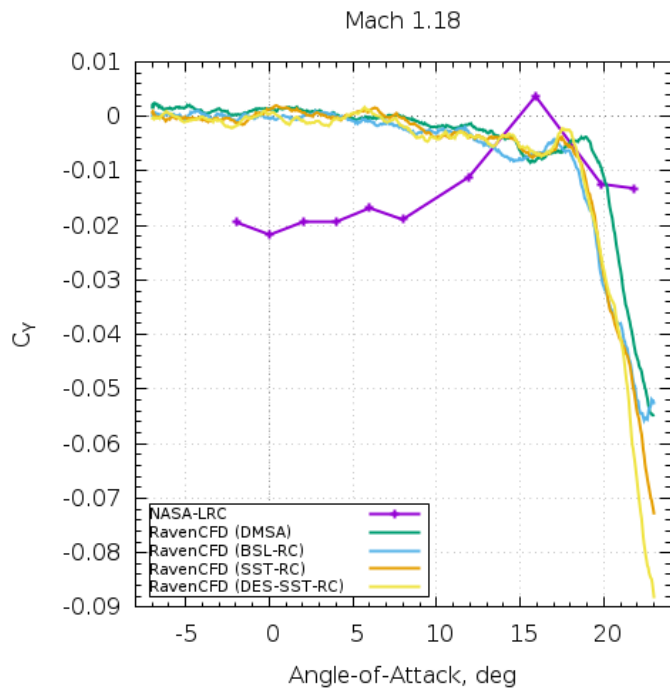
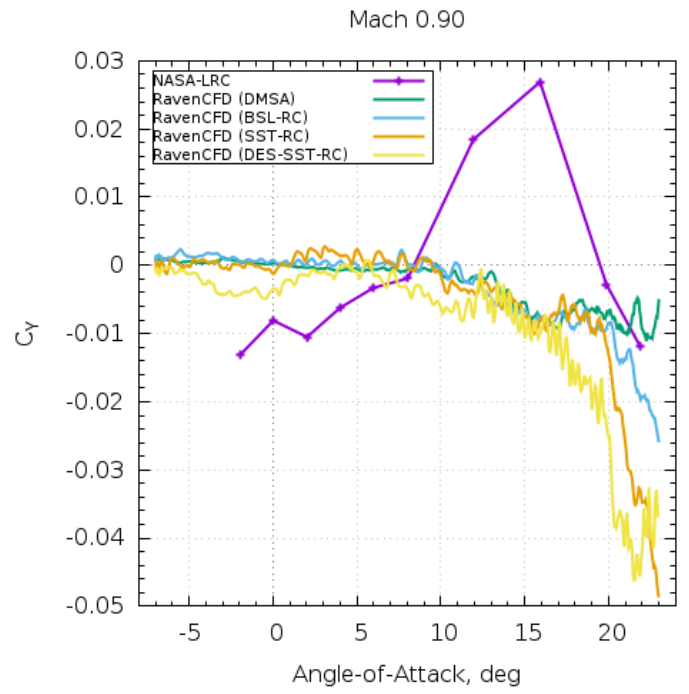
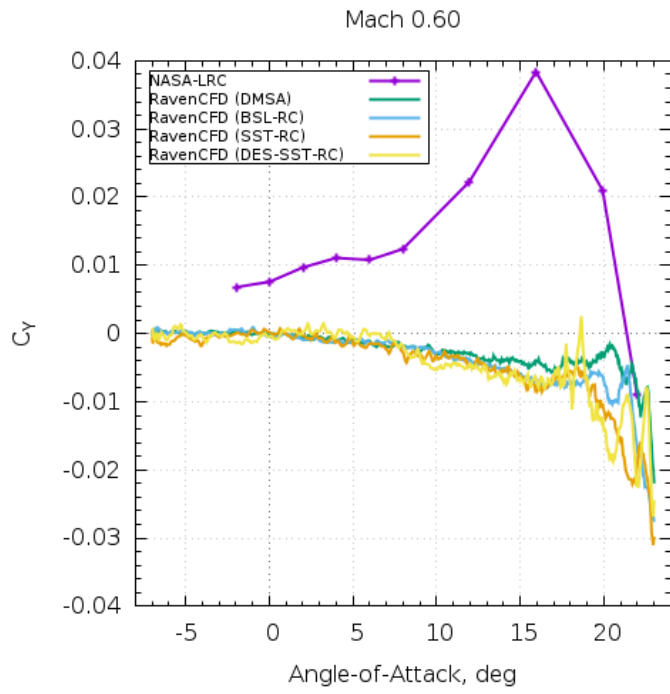
Table 4. RavenCFD Run Matrix

Run Number	Configuration Number	$\alpha_i$	$\alpha_f$	$\beta$	$\phi$	$u'/\delta$	$M_\infty$	$p_\infty$	$T_\infty$	Turbulence Modeling Approach
00001	2	-7	23	0	0	0/0/0	<b>0.601</b>	5.458	540.8	<b>DMSA</b>
00002	2	-7	23	0	0	0/0/0	<b>0.900</b>	3.292	499.7	<b>DMSA</b>
00003	2	-7	23	0	0	0/0/0	<b>1.185</b>	2.196	452.7	<b>DMSA</b>
00004	2	-7	23	0	0	0/0/0	<b>2.000</b>	0.835	324.8	<b>DMSA</b>
00005	2	-7	23	0	0	0/0/0	<b>0.601</b>	5.458	540.8	<b>BSL-RC</b>
00006	2	-7	23	0	0	0/0/0	<b>0.900</b>	3.292	499.7	<b>BSL-RC</b>
00007	2	-7	23	0	0	0/0/0	<b>1.185</b>	2.196	452.7	<b>BSL-RC</b>
00008	2	-7	23	0	0	0/0/0	<b>2.000</b>	0.835	324.8	<b>BSL-RC</b>
00009	2	-7	23	0	0	0/0/0	<b>0.601</b>	5.458	540.8	<b>SST-RC</b>
00010	2	-7	23	0	0	0/0/0	<b>0.900</b>	3.292	499.7	<b>SST-RC</b>
00011	2	-7	23	0	0	0/0/0	<b>1.185</b>	2.196	452.7	<b>SST-RC</b>
00012	2	-7	23	0	0	0/0/0	<b>2.000</b>	0.835	324.8	<b>SST-RC</b>
00013	2	-7	23	0	0	0/0/0	<b>0.601</b>	5.458	540.8	<b>DES-SST-RC</b>
00014	2	-7	23	0	0	0/0/0	<b>0.900</b>	3.292	499.7	<b>DES-SST-RC</b>
00015	2	-7	23	0	0	0/0/0	<b>1.185</b>	2.196	452.7	<b>DES-SST-RC</b>
00016	2	-7	23	0	0	0/0/0	<b>2.000</b>	0.835	324.8	<b>DES-SST-RC</b>

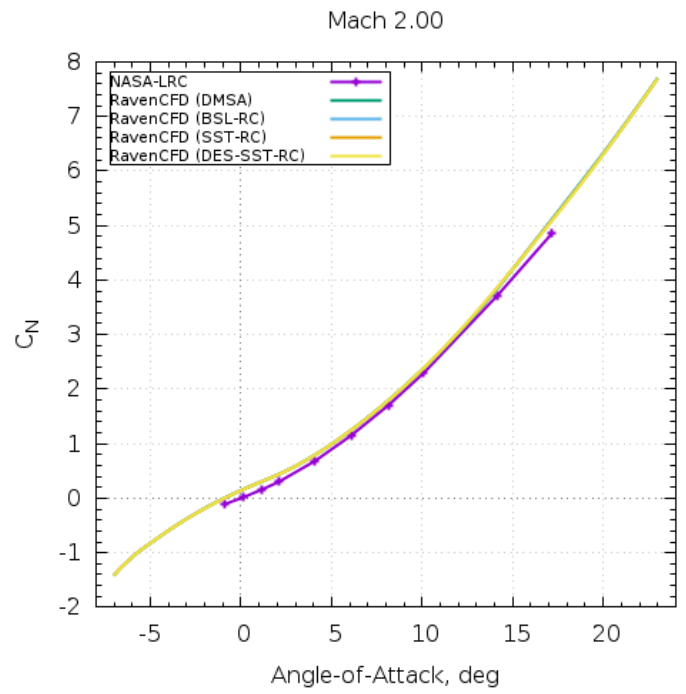
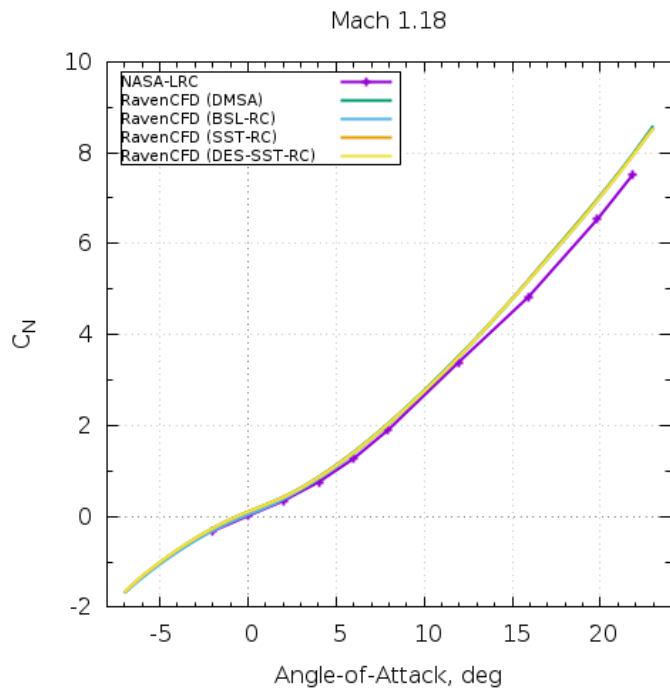
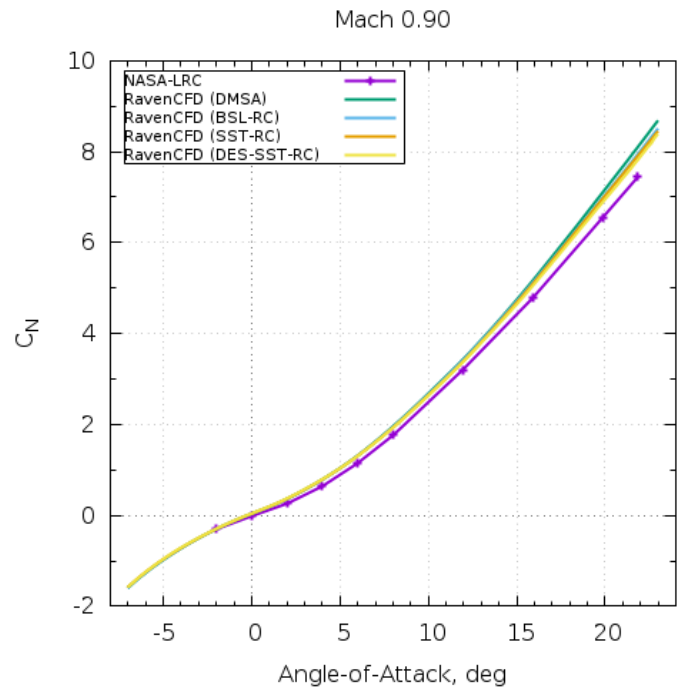
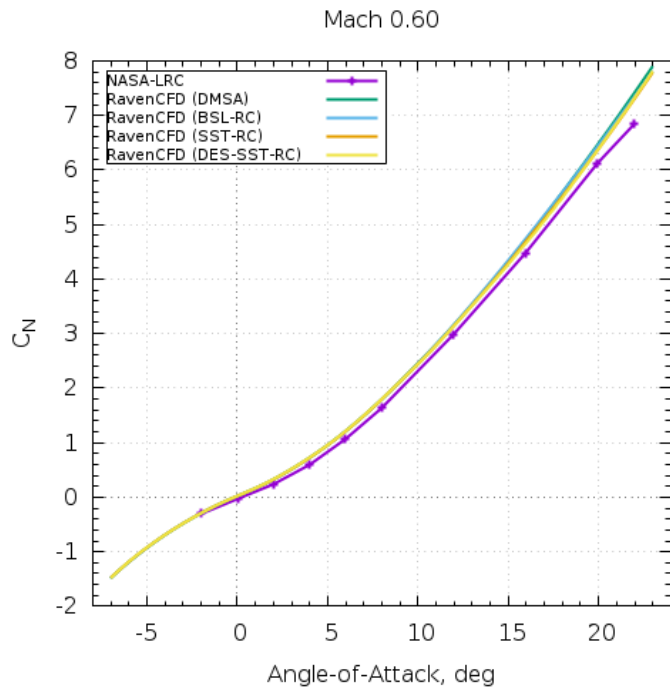
## B. Axial Force Coefficient Plots



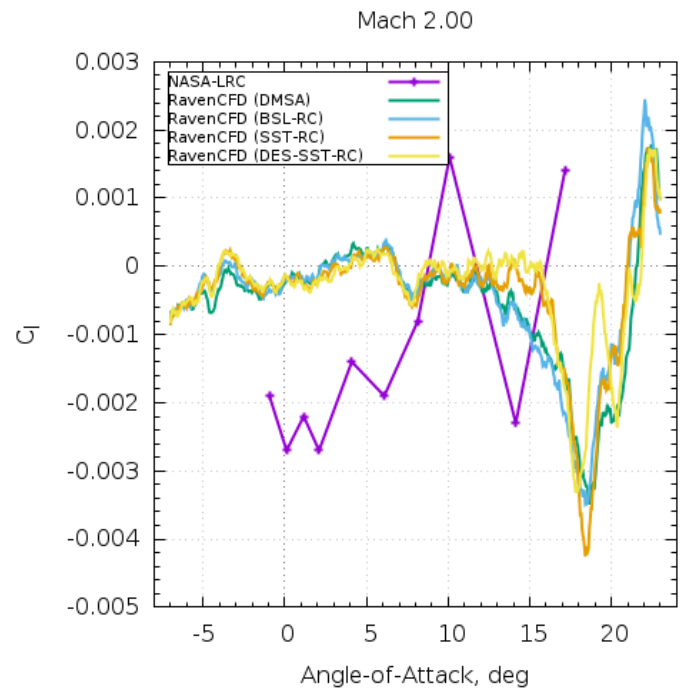
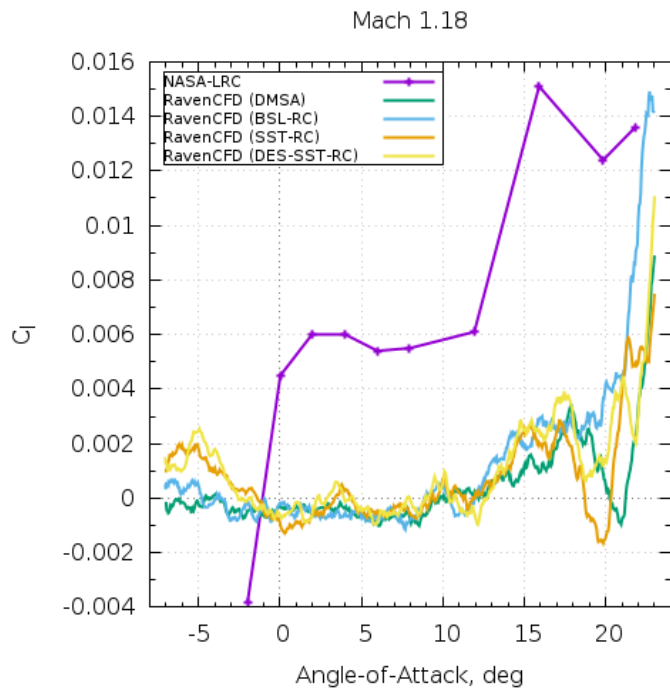
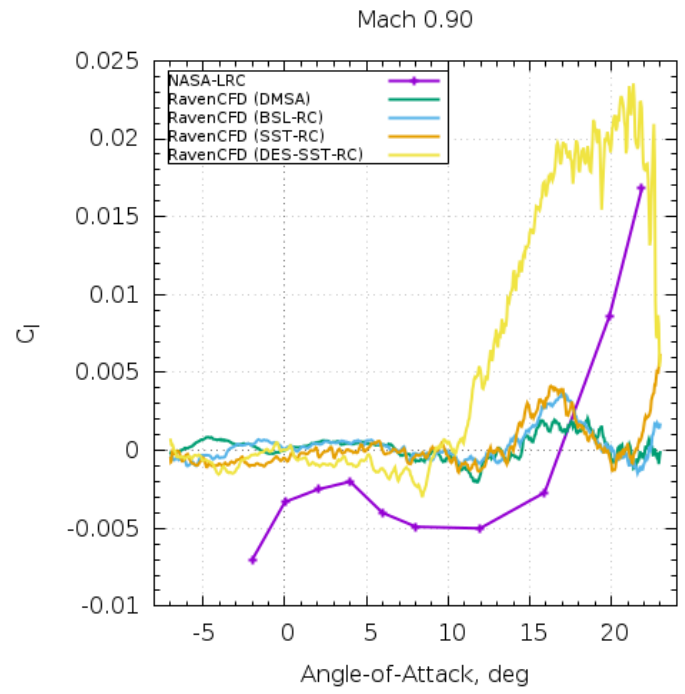
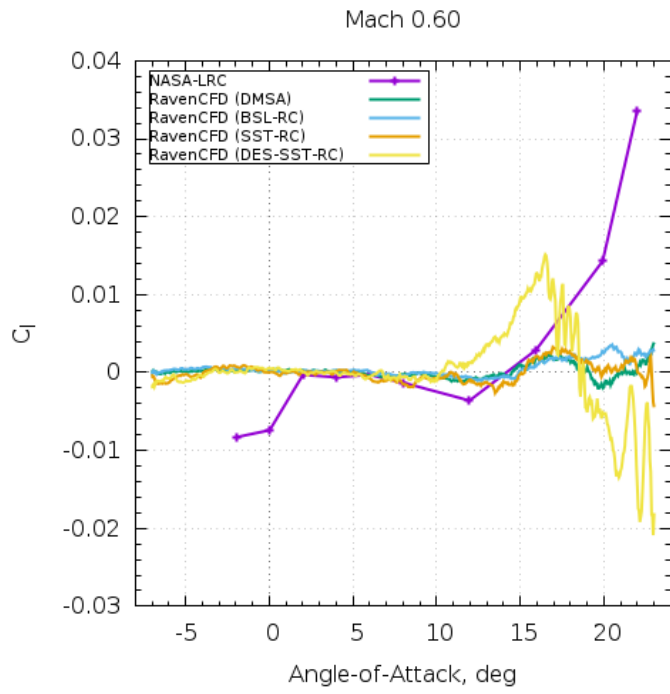
### C. Side Force Coefficient Plots



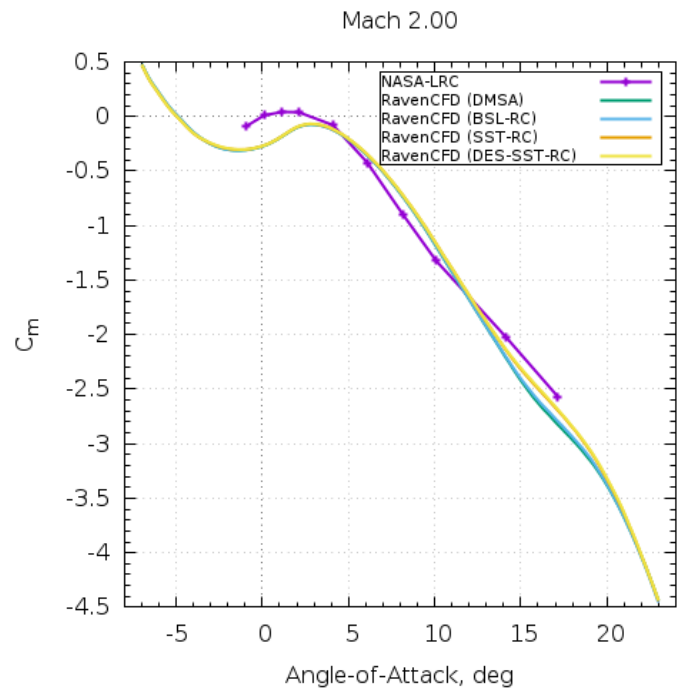
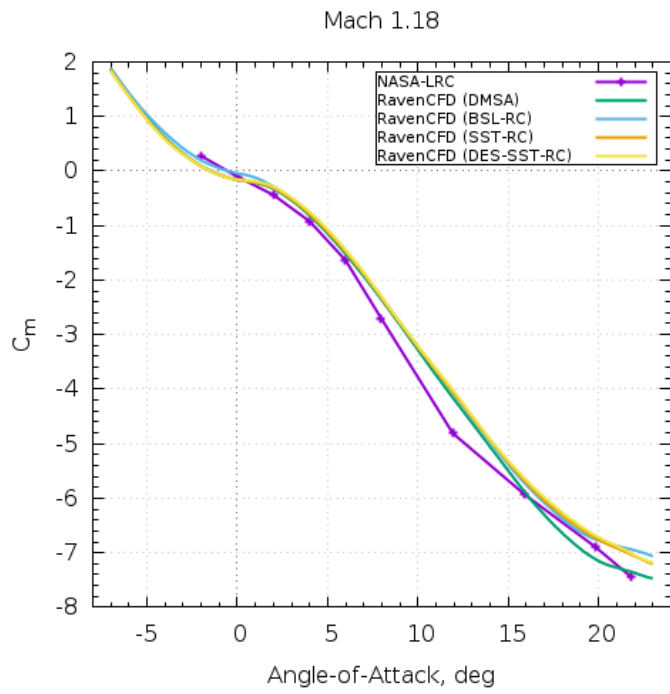
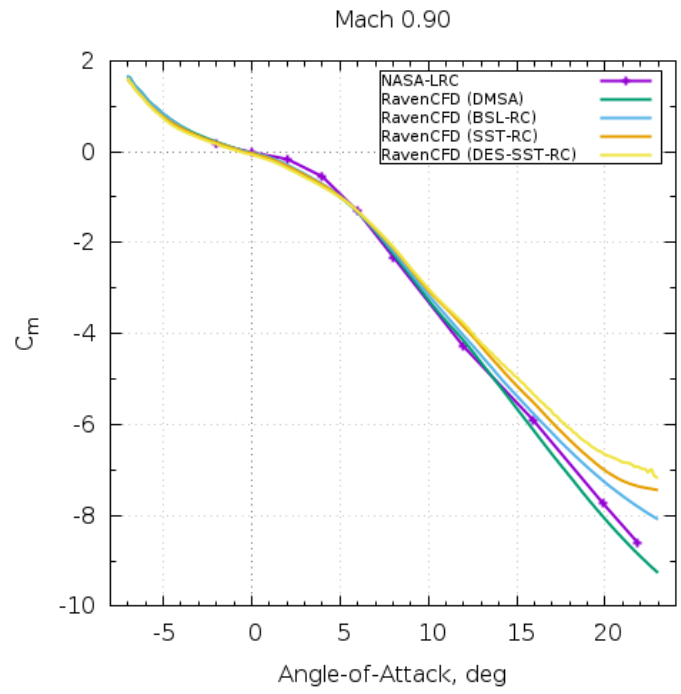
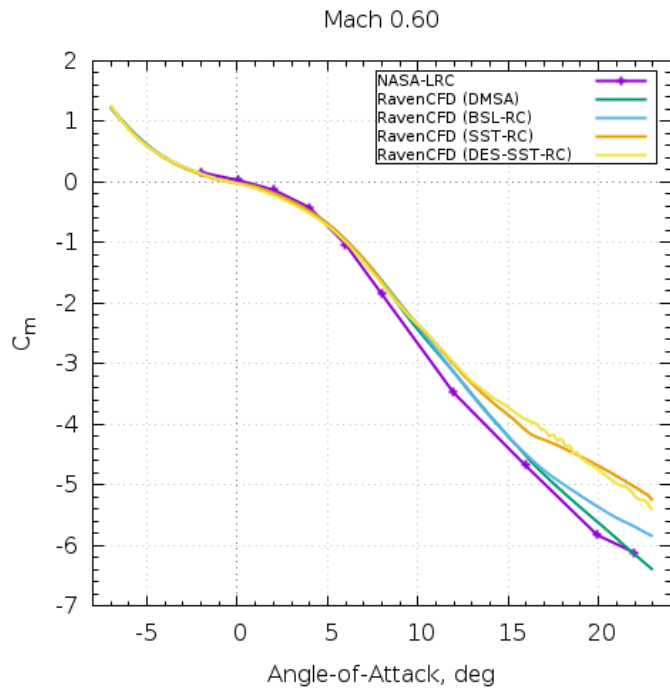
## D. Normal Force Coefficient Plots



## E. Rolling Moment Coefficient Plots

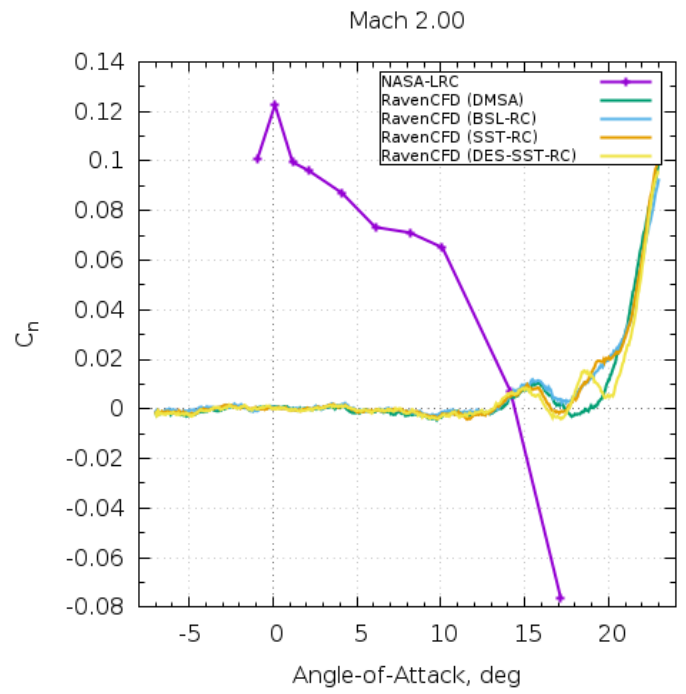
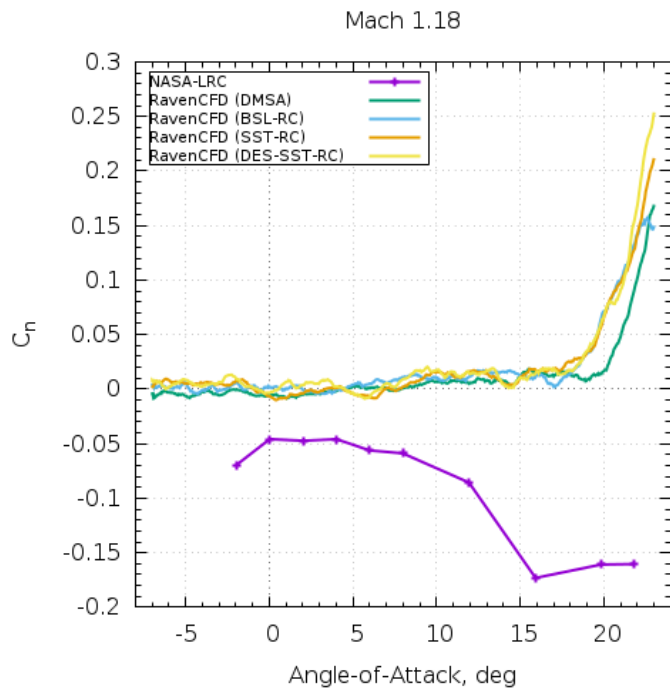
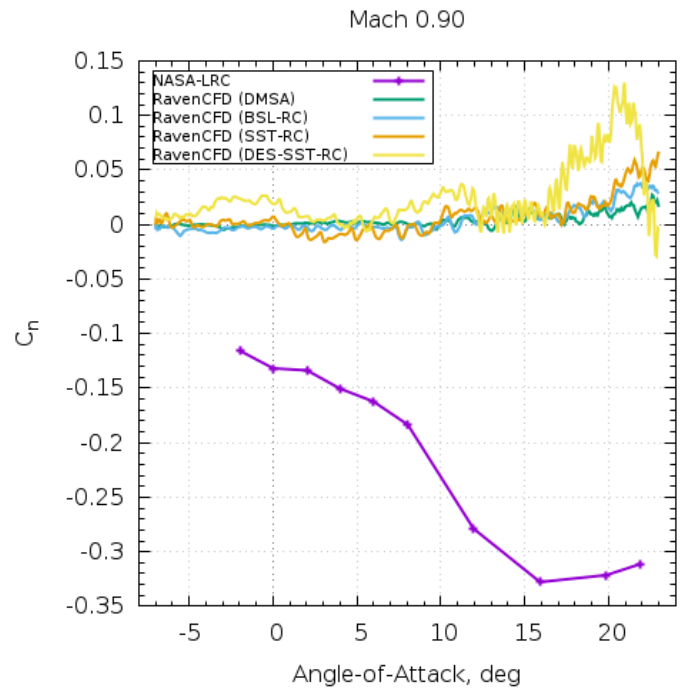
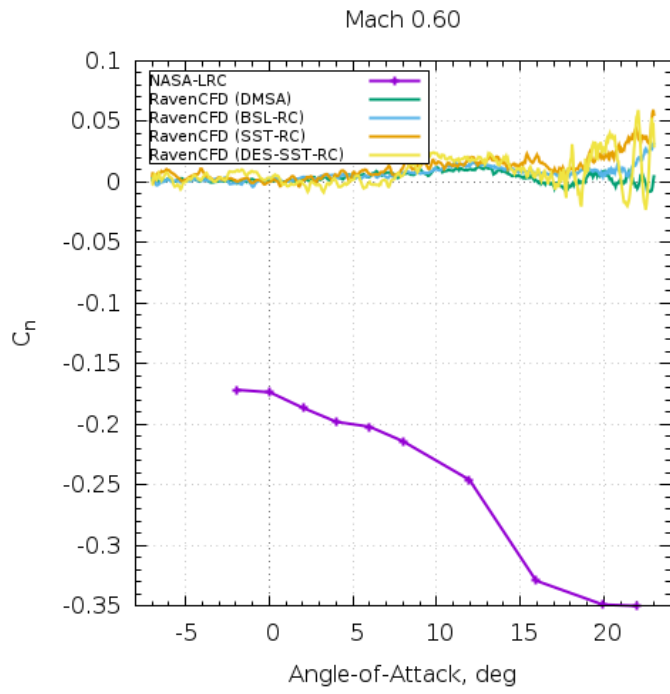


## F. Pitching Moment Coefficient Plots





## G. Yawing Moment Coefficient Plots



## Acknowledgments

*I would sincerely like to thank Gregory Z. McGowan, Ph.D. and the Standard Missile Group at Corvid Technologies LLC for their support and dedication to this study as well as Corvid Technologies LLC, who provided the supercomputing resources used throughout this study.*

## References

- [1] Strelets, M., "Detached Eddy Simulation of Massively Separated Flows," 39th Aerospace Sciences Meeting and Exhibit, Aerospace Sciences Meetings, 2001.  
doi:10.2514/6.2001-879
- [2] Smagorinsky, J., "General Circulation Experiments with the Primitive Equations, Part I: The Basic Experiment," Monthly Weather Review, 1963.
- [3] Kolmogorov, A. N., "The Local Structure of Turbulence in Incompressible Viscous Fluid for Very Large Reynolds Number," C.R. Acad. Sci. U.S.S.R., 1941.
- [4] Allen, J. M., "Aerodynamics of an Axisymmetric Missile Concept Having Cruciform Strakes and In-Line Tail Fins from Mach 0.60 to 4.63," NASA Langley Research Center, 2005. NASA TM-2005-213541.
- [5] Edwards, J. R., "A Low-Diffusion Flux-Splitting Scheme for Navier-Stokes Calculations," Computers & Fluids, Vol. 26, No. 6, 1997, pp. 635-659.  
doi:10.1016/S0045-7930(97)00014-5
- [6] Dacles-Mariani, J., Zilliac, G. G., Chow, J. S., and Bradshaw, P., "Numerical/Experimental Study of a Wingtip Vortex in the Near Field," AIAA Journal, Vol. 33, No. 9, 1995, pp. 1561-1568.
- [7] Dacles-Mariani, J., Kwak, D., and Zilliac, G. G., "On Numerical Errors and Turbulence Modeling in Tip Vortex Flow Prediction," Int. J. for Numerical Methods in Fluids, Vol. 30, 1999, pp. 65-82.
- [8] Menter, F. R., "Two-Equation Eddy-Viscosity Turbulence Models for Engineering Applications," AIAA Journal, Vol. 32, No. 8, August 1994, pp. 1598-1605.
- [9] Smirnov, P. E., Menter, F. R., "Sensitization of the SST Turbulence Model to Rotation and Curvature by Applying the Spalart-Shur Correction Term," ASME Journal of Turbomachinery, Vol. 131, October 2009, 041010.

